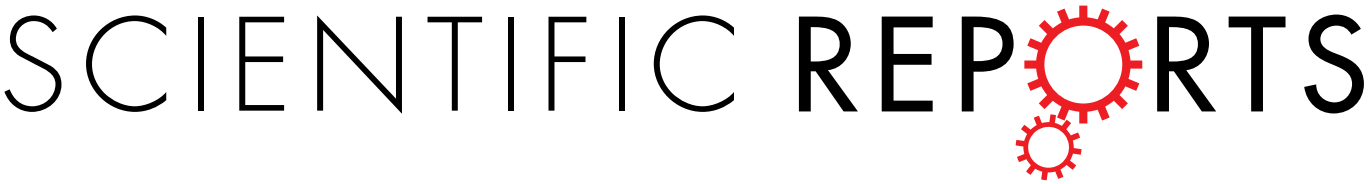

OPEN

Mn-induced Ferromagnetic Semiconducting Behavior with Linear Negative Magnetoresistance in $Sr_4(Ru_{1-x}Mn_x)_3O_{10}$ Single Crystals

Received: 29 May 2018
Accepted: 24 August 2018
Published online: 06 September 2018

Lingyi Xing[1], Xin Gui[2], Weiwei Xie[2], Huibo Cao[3], Jiaqiang Yan[4], Brian C. Sales[4] & Rongying Jin[1]

Triple-layered $Sr_4Ru_3O_{10}$ is a unique ferromagnet with the central RuO_6 layer behaving differently from two outer layers both crystallographically and magnetically. We report that the partial substitution of Ru by smaller Mn gives rise to modification in crystal structure, electronic and magnetic properties of $Sr_4(Ru_{1-x}Mn_x)_3O_{10}$. Through the single crystal X-ray diffraction refinement, we find that (Ru/Mn)O_6 octahedral rotation is no longer detectable at $x \geq 0.23$, leading to the tetragonal structure. The magnetization measurements indicate the ferromagnetic transition temperature T_C decreases from 105 K for $x = 0$ to 30 K for $x = 0.41$, with the reduced magnetic moment as well. Remarkably, Mn doping results in the change of magnetic anisotropy from the easy *c* axis in $x = 0$ to the easy *ab* plane seen in $x = 0.34$ and 0.41. Such change also removes the *ab*-plane metamagnetic transition observed in $x = 0$. Furthermore, the electrical resistivity increases with increasing *x* showing semiconducting behavior with $\Delta \sim 10$ meV for $x = 0.34$ and 30 meV for $x = 0.41$. Under applied magnetic field, the magnetoresistance exhibits negative and linear field dependence in all current and field configurations. These results clearly indicate $Sr_4(Ru_{1-x}Mn_x)_3O_{10}$ is a novel ferromagnetic semiconductor with exotic magnetotransport properties.

The Ruddlesden-Popper (RP) ruthenates $Sr_{n+1}Ru_nO_{3n+1}$ ($n = 1, 2, 3 \ldots \infty$) have attracted great attention because of their exotic electronic and magnetic properties. While the only difference in their chemical composition is the number of RuO_6 octahedral layers *n* in the unit cell, their physical properties vary from a *p*-wave superconductor ($n = 1$)[1], to a paramagnetic metal with magnetic field-induced quantum critical point ($n = 2$)[2], to an unusual ferromagnetic metal with in-plane metamagnetism ($n = 3$)[3], to a ferromagnetic polar metal ($n = \infty$)[4]. Both experimental[3,5–10] and theoretical studies[10–12] indicate that the fundamental building block RuO_6 octahedron plays an extremely important role in these unconventional properties. In the RP series, RuO_6 octahedra are connected by corner sharing O atoms within the *n* layers, which can be distorted in multiple ways such as elongation, compression, rotation, and tilt. For example, with increasing *n*, the rotation angle of RuO_6 octahedron changes from zero ($n = 1$)[13], to 7° ($n = 2$)[14,15], to 11.2° ($n = 3$)[16] to ~12° ($n = \infty$). According to theoretical calculations[11,17,18], such distortion impacts the electronic distribution, thus changing the physical properties.

In the RP series, the members with odd *n* are particularly interesting. For Sr_2RuO_4 with $n = 1$, the RuO_6 octahedron rotates about 9° at the surface[10], even it is absent in bulk. Such rotation may stabilize ferromagnetism at the surface, which is ultimately connected to the Cooper pair formation with parallel spins in bulk. For $Sr_4Ru_3O_{10}$ with $n = 3$, the RuO_6 octahedron in the central layer apparently rotates double amount (~11.2°) than that in the two outer layers (~5.6°), corresponding to different magnetic moment as well[16]. According to density functional calculations[11,12], the orthorhombic structure with the rotation of the RuO_6 octahedron is in favor of ferromagnetic coupling. In the previous study of $Sr_3(Ru_{1-x}Mn_x)_2O_7$, partial replacement of Ru by smaller Mn leads to the decrease of (Ru/Mn)O_6 octahedral rotation, and long-range antiferromagnetic (AFM) ordering at T_N[8]. Intriguingly, T_N versus *x* is dome-like with both T_N and the rotation vanishes at the same doping level. This

[1]Department of Physics and Astronomy, Louisiana State University, Baton Rouge, LA, 70803, USA. [2]Department of Chemistry, Louisiana State University, Baton Rouge, LA, 70803, USA. [3]Neutron Scattering Division, Oak Ridge National Laboratory, Oak Ridge, TN, 37831, USA. [4]Materials Science and Technology Division, Oak Ridge National Laboratory, Oak Ridge, TN, 37831, USA. Correspondence and requests for materials should be addressed to R.J. (email: rjin@lsu.edu)

Atom	Wyckoff.	Occupancy.	*x*	*y*	*z*	U_{eq}
Sr1	4*e*	1	0	0	0.43011 (4)	0.0092 (3)
Sr2	4*e*	1	0	0	0.29737 (4)	0.0074 (3)
(Ru/Mn) 1	4*e*	0.784 (8)/0.216	½	½	0.35987 (3)	0.0045 (3)
(Ru/Mn) 2	2*a*	0.741 (8)/0.259	½	½	½	0.0033 (4)
O1	4*e*	1	½	½	0.2896 (2)	0.009 (2)
O2	4*e*	1	½	½	0.4310 (4)	0.016 (2)
O3	8*g*	1	½	0	0.3610 (2)	0.014 (1)
O4	4*c*	1	½	0	½	0.043 (4)

Table 1. Atomic coordinates and equivalent isotropic displacement parameters of $Sr_4(Ru_{0.77(1)}Mn_{0.23})_3O_{10}$ at 300 (2) K obtained through single crystal X-ray diffraction refinement. U_{eq} is defined as one-third of the trace of the orthogonalized U_{ij} tensor (Å^2).

Atom	Wyckoff.	Occupancy.	*x*	*y*	*z*	U_{eq}
Sr1	4*e*	1	0	0	0.43022 (4)	0.0093 (3)
Sr2	4*e*	1	0	0	0.29779 (3)	0.0076 (3)
(Ru/Mn)1	4*e*	0.596(8)/0.404	½	½	0.35989 (3)	0.0045 (3)
(Ru/Mn)2	2*a*	0.575(8)/0.425	½	½	½	0.0034 (4)
O1	4*e*	1	½	½	0.2906 (2)	0.010 (2)
O2	4*e*	1	½	½	0.4309 (2)	0.014 (2)
O3	8*g*	1	½	0	0.3609 (2)	0.012 (1)
O4	4*c*	1	½	0	½	0.038 (3)

Table 2. Atomic coordinates and equivalent isotropic displacement parameters of $Sr_4(Ru_{0.59(1)}Mn_{0.41})_3O_{10}$ at 300(2)K obtained through single crystal X-ray diffraction refinement. U_{eq} is defined as one-third of the trace of the orthogonalized U_{ij} tensor (Å^2).

suggests that the correlation between octahedral rotation and magnetic coupling is more complex than simple monotonic response. Given its magnetic ground state and the difference in local structure between outer and central layers[19,20], $Sr_4Ru_3O_{10}$ could be much more susceptible to Mn doping than the case of n = 2. In this article, we report, for the first time, the experimental investigation of Mn doped $Sr_4Ru_3O_{10}$ single crystals, including the crystal structure, magnetization, and electrical transport properties. The partial replacement of Ru by Mn results in the modification of (1) crystal structure by removing octahedral rotation, (2) magnetic interaction by changing the easy axis from the *c* direction to the *ab* plane, and (3) electrical conduction from metallic to semiconducting with unusual magnetotransport behavior.

Results and Discussion

For both nominal $x = 0.25$ and 0.5 crystals, our single-crystal X-ray diffraction refinement results in structural and compositional information that are given in Tables 1 and 2, respectively. The refinement indicates that they form a tetragonal structure (S.G. I4/mmm) with actual $x = 0.23$ and 0.41, respectively. Note that the actual Mn concentration is the average value of Mn in the central layer (Mn1) and outer layers (Mn2). While Mn is randomly distributed within each layer, our structural refinement indicates that Mn1 concentration is slightly lower than Mn2 in both $x = 0.23$ and 0.41. As summarized in Tables 1 and 2 for $x = 0.23$ and 0.41, the atomic coordination and occupancy correspond to the $Sr_4(Ru_{1-x}Mn_x)_3O_{10}$ phase with lattice parameters $a = b = 3.9033(5)$ Å and $c = 28.138(3)$ Å for $x = 0.23$, and $a = b = 3.910(4)$ Å and $c = 27.96(3)$ Å for $x = 0.41$. The doping concentration *x* obtained from XRD is consistent with the element analysis through wavelength dispersive spectroscopy (WDS) via Joel JXA-8230 Electron Microprobe. The WDS measurements of nominal $x = 0.4$ single crystals give actual $x = 0.34$, which are used for the investigations of electrical and magnetic properties presented below.

Figure 1(a) depicts the crystal structure of $Sr_4(Ru_{1-x}Mn_x)_3O_{10}$ for $x = 0.23$ and 0.41, with the indication of two Ru/Mn ((Ru/Mn)1 and (Ru/Mn)2) sites and four O (O1, O2, O3, O4) sites. Compared to the undoped case ($x = 0$) as shown in the right of Fig. 1(a), both the number of Ru/Mn and O sites are reduced. The change from orthorhombic for x = 0 to tetragonal for $x = 0.23$, and 0.41 indicates the removal of octahedral rotation upon Mn doping. While *a* (*b*) (the values for parent compound are divided by $\sqrt{2}$) remains more or less a constant, lattice parameter *c* decreases with increasing *x* as plotted in Fig. 1(b). This means that the unit cell volume decreases with increasing *x* (see the inset of Fig. 1(b)). To understand the origin of unit cell shrinkage, we plot the *x* dependence of the bond lengths of Ru/Mn-O in four different octahedra (I, II, III and IV, referred from $x = 0$) in Fig. 1(c–f), respectively. With increasing *x*, while the in-plane bond length slightly decreases, the out-of-plane Ru/Mn-O bond length decreases more dramatically. By calculating the ratio of the average out-of-plane to in-plane Ru/Mn-O distance, we obtain the *x* dependence of the Jahn-Teller (JT) distortion δ_{JT} for I, II, III and IV, which are shown in Fig. 1(g). Note that δ_{JT} for outer-layer octahedra (I and III) decrease from 1.05 to 1.00 while those for central-layer octahedra (II and IV) decrease from 1.01 to 0.99, as *x* increases from 0 to 0.41. These indicate Mn doping makes the outer-layer octahedra less elongated, and the central-layer ones slightly compressed.

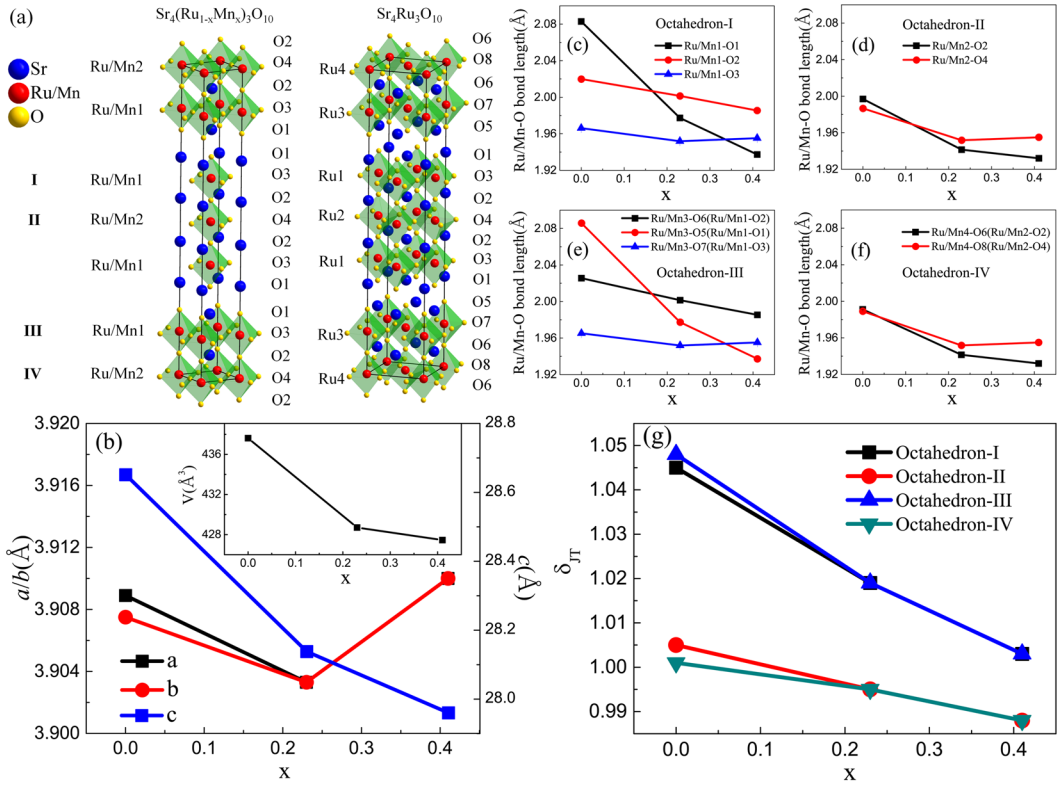

Figure 1. (**a**) Crystal structure of $Sr_4(Ru_{1-x}Mn_x)_3O_{10}$ ($x = 0.23$ and 0.41) (left) and the parent compound $Sr_4Ru_3O_{10}$ (right)[3]. (**b**) Doping (x) dependence of lattice parameters a, b, and c. For $x = 0$, $a/\sqrt{2}$ and $b/\sqrt{2}$ are used. The inset is the x dependence of the unit cell volume V. (**c**–**f**) Doping (x) dependence of the Bond lengths of (Ru/Mn)-O in four different octahedral. (**g**) Doping (x) dependence of the Jahn-Teller distortion δ_{JT} for four different octahedra.

Figure 2(a,b) show the temperature dependence of the magnetic susceptibility for $x = 0.34$ and 0.41 measured with H (= 1 T) parallel to the ab plane (χ_{ab}) and c axis (χ_c), respectively. While the overall profile is similar to that observed in $x = 0$[3], several features are worth noting: (1) both χ_{ab} and χ_c only reflect one magnetic transition T_C, which is 35 K for $x = 0.34$ and 30 K for $x = 0.41$; (2) $\chi_{ab} > \chi_c$ for $x = 0.34$ and 0.41, indicating that the magnetic easy axis is along the ab plane. Compared to the case of $x = 0$, T_C obviously is decreased and the magnetic easy axis is switched from the c direction to the ab plane upon Mn doping. In analyzing the high temperature susceptibility data using the Curie–Weiss law $\chi = \chi_0 + \frac{N_A \mu_{eff}^2 / 3k_B}{T - \theta_{CW}}$ (χ_0 is a constant, N_A is the Avogadro constant, and k_B the Boltzmann constant), we obtain positive Curie-Weiss temperature θ_{CW} and effective moment μ_{eff}. For $x = 0.34$, $\chi_0 \sim -0.003$ emu/mol, $\theta_{CW} \sim 33$ K and $\mu_{eff} \sim 3.4\mu_B$, and $\chi_0 \sim -0.01$ emu/mol, $\theta_{CW} \sim 37$ K and $\mu_{eff} \sim 3.2\mu_B$ for $x = 0.41$. The positive θ_{CW} value indicates that magnetic interaction is ferromagnetic along both the ab plane and c axis, similar to the $x = 0$ case[3]. However, for $x = 0.41$, θ_{CW} is higher than T_C, which usually occurs in low-dimensional or frustrated magnetic systems. While there is little anisotropy in magnetic susceptibility above θ_{CW}, the tetragonal structure disfavors magnetic frustration as well. One possibility is that the compressed central $(Ru/Mn)O_6$ layer [see Fig. 1(g)] may be in favor of antiferromagnetic interaction, while the elongated two outer $(Ru/Mn)O_6$ layers support ferromagnetic interaction according to theoretical calculations[11,12]. The mixed ferromagnetic and antiferromagnetic interactions result in higher θ_{CW} but smaller μ_{eff} in $x = 0.41$ compared to the case of $x = 0.34$. Although similar argument also should apply to the latter case, antiferromagnetic interaction is less dramatic own to smaller or close-to-zero compression of the central $(Ru/Mn)O_6$ octahedra [see Fig. 1(g)]. Nevertheless, the estimated μ_{eff} for $x = 0.34$, and 0.41 corresponds to effective spin $1 < S_{eff} \sim 1.19–1.28 < 3/2$ for Ru/Mn, slightly higher than the undoped case with $S = 1$[21]. This suggests that Mn has the same valence as Ru^{4+}, i.e., Mn^{4+}, which gives $S = 3/2$.

To further identify the nature of the magnetic interaction in the doped systems, the magnetization hysteresis is measured at various temperatures, which is presented in Fig. 2(c–f) for both $x = 0.34$ and 0.41 with $H//ab$ and $H//c$, respectively. In both directions, $M(H)$ is linear at high temperatures for $x = 0.34$ and 0.41. As temperature is lowered, non-linear $M(H)$ is observed at low fields as seen at $T = 80$ K. However, the hysteresis loop does not occur until T approaches T_C, consistent with long-range ferromagnetic ordering. More importantly, there is no sudden increase upon increasing magnetic field in either M_{ab} or M_c. This indicates the absence of the metamagnetic transition up to 7 Tesla in both $x = 0.34$ and 0.41. Furthermore, the magnetic moment at 7 T decreases with increasing Mn doping level, consistent with the scenario that Mn doping increases antiferromagnetic interaction.

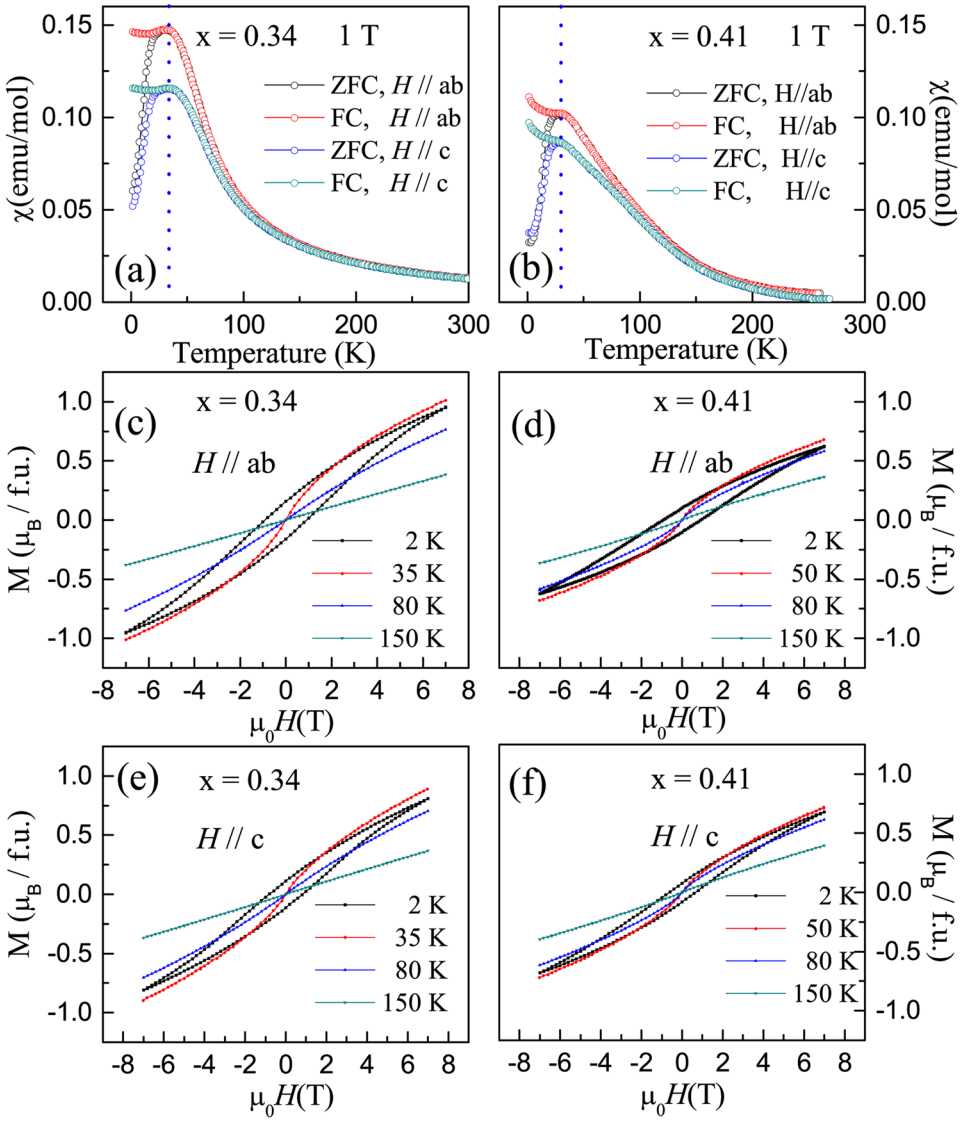

Figure 2. (**a**,**b**) Temperature dependence of the magnetic susceptibility χ for $x = 0.34$ and 0.41 single crystals measured by applying $H = 1$ T alongThe Ruddlesden-Popper (RP) ruthenates the *ab* plane and *c* axis, respectively. The blue dotted lines represent the ferromagnetic transition temperature. (**c**,**d**) Magnetization hysteresis loops at different temperatures for $x = 0.34$ and 0.41 single crystals when *H*//*ab*. (**e**,**f**) Magnetization hysteresis loops at different temperatures for $x = 0.34$ and 0.41 single crystals when *H*//*c*.

According to previous studies, small percentage of Mn doping in single-layered Sr_2RuO_4 (n = 1)[22] and double-layered $Sr_3Ru_2O_7$ (n = 2)[8,23] results in antiferromagnetic insulating ground state. The same trend is observed in $SrRuO_3$ (n = ∞), in which more than 39% Mn doping turns the system into an AFM insulator as well[24,25]. The fact that $Sr_4(Ru_{1-x}Mn_x)_3O_{10}$ ($x = 0.34$ and 0.41) retains its ferromagnetic (FM) ordering is remarkable, suggesting that the magnetic interaction in the n = 3 system is different from those mentioned above. Figure 3(a–e) show temperature dependence of both in-plane (ρ_{ab}) and c-axis (ρ_c) resistivities for $x = 0.34$ (a–c) and 0.41 (d–e), respectively. Note that, for $x = 0.34$, ρ_c shows a semiconducting behavior in the entire measured temperature range while the metal-insulator transition (MIT) temperature occurs at 215 K in the *ab*-plane (see Fig. 3(c)). For $x = 0.41$, we can speculate that this transition is beyond 300 K, as both ρ_{ab} and ρ_c are non-metallic below 300 K. While no anomaly is observed in ρ_{ab} and ρ_c at T_C, the resistivity anisotropy ρ_c/ρ_{ab}, presented in Fig. 3(f), shows steep change below T_C than that at higher temperatures. This is consistent with the magnetic anisotropy that stronger in-plane ferromagnetism ($M_{ab} > M_c$) results in better electrical conduction along the *ab* plane. By replotting the temperature dependence of resistivities as lnρ versus T^{-1} in the inset of Fig. 3(a,b,d and e), liner relationship is clearly revealed. This indicates that both $\rho_{ab}(T)$ and $\rho_c(T)$ can be described by the thermal activation model $\rho = \rho_0 \exp(\Delta/k_BT)$, where ρ_0 is a temperature-independent constant, and Δ is the thermal activation energy. By fitting experimental data to the formula, we obtain $\Delta \sim 10$ meV and 30 meV for $x = 0.34$ and 0.41, respectively. The solid lines in the insets of Fig. 3(a,b,d and e) represent the fitting results, which describe the experimental data very well.

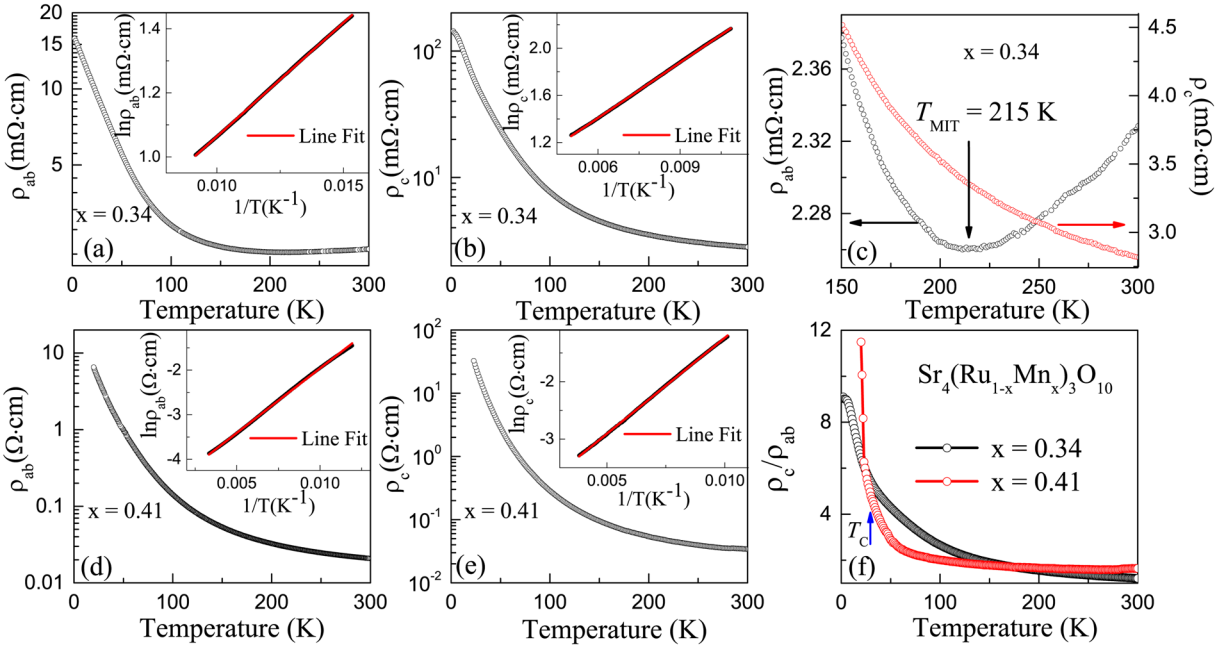

Figure 3. The temperature dependence of (**a**) the *ab*-plane resistivity ρ_{ab} and (**b**) the *c*-axis resistivity ρ_c, and (**c**) the enlarged ρ_{ab} and ρ_c for $x = 0.34$ single crystal. The temperature dependence of (**d**) the *ab*-plane resistivity ρ_{ab} and (**e**) the *c*-axis resistivity ρ_c for $x = 0.41$ single crystal, and (**f**) the anisotropy ρ_c/ρ_{ab}. The insets for both (**a**,**b**,**d**) and (**e**) show the replot of $\rho_{ab}(T)$ and $\rho_c(T)$, and fitting curves (red) according to the thermal activation model $\rho = \rho_0 \exp(\Delta/\kappa_B T)$.

The above electrical and magnetic properties indicate that the Mn-doped $Sr_4(Ru_{1-x}Mn_x)_3O_4$ ($x = 0.34$ and 0.41) is a *ferromagnetic semiconductor with a narrow energy gap*. This sets it apart from other sister compounds with Mn doping and adds a new member in a small magnetic semiconductor family. Further evidence for ferromagnetic semiconducting properties of $Sr_4(Ru_{1-x}Mn_x)_3O_4$ ($x = 0.34$ and 0.41) is reflected in magnetoresistance (MR). Figure 4(a–d) show, for $x = 0.34$, the field dependence of the MR for $I//ab$ and $H//I$ ($MR_{ab}^{//}$), $I//ab$ and $H \perp ab$ ($MR_{ab}^{\perp}$), $I//c$ and $H//c$ ($MR_c^{//}$), and $I//c$ and $H \perp c$ ($MR_c^{\perp}$), respectively. Several features are worth noting. First, the MR in all field and current configurations is *negative* at $T \leq 150$ K. Second, $|MR_{ab}^{//}| > |MR_{ab}^{\perp}|$ and $|MR_c^{\perp}| > |MR_c^{//}|$. Third, MR measured in all configurations exhibits more or less linear field dependence without the sign of saturation up to 14 Tesla. The same features also are observed for $x = 0.41$ as shown in Fig. 4(e–h).

The negative MR for $Sr_4(Ru_{1-x}Mn_x)_3O_4$ ($x = 0.34$ and 0.41) is different from that seen in the parent compound, which is positive along both the *ab* plane and *c* direction prior to the metamagnetic transition field[26,27]. This confirms that the magnetic properties of Mn-doped system are different from the undoped case. Furthermore, the fact that $|MR_{ab}^{//}| > |MR_{ab}^{\perp}|$ and $|MR_c^{\perp}| > |MR_c^{//}|$ indicate that spin scattering is strong in the *ab* plane, and can be more effectively suppressed when $H//ab$. This is consistent with the observation that the magnetic easy axis in $Sr_4(Ru_{1-x}Mn_x)_3O_4$ ($x = 0.34$ and 0.41) is along the *ab* plane. The most remarkable feature is the linear-*H* dependence of negative MR in all configurations. While it is discussed in both classic and quantum scenarios, linear negative MR (LNMR) in all configurations is rare.

In normal circumstances, one would expect that MR exhibits the H^2 dependence in low fields and eventually saturates at high fields[28]. Linear MR can be found in materials with open Fermi surfaces[29], disordered metals or semiconductors[30–33], and in the extreme quantum limit with $\hbar\omega_c > E_F$ (where ω_c is the cyclotron frequency and E_F is the Fermi energy)[34–36]. However, the MR is usually positive in these scenarios. LNMR has been discussed in non-magnetic disordered 2D gas systems with random corrugation and defects[37–41], and polycrystalline graphite consisting of nano-sized particles[42]. In the latter case, the system exhibits semiconducting behavior with thermally activated electrical conduction. Due to its polycrystalline nature, it consists of weak localization (WL)[43] and diffuse scattering (DS) between grain boundaries[44], giving rise to $MR_{total} = MR_{WL} + MR_{DS} = -K_1H^{1/2} - K_2H^2$ (K_1 and K_2 are constants)[42]. Experimentally, one would observe LNMR as the consequence of these two contributions. As T approaches 0 K, MR_{WL} becomes dominant, leading to cusp-shaped H dependence of MR. While $Sr_4(Ru_{1-x}Mn_x)_3O_{10}$ exhibits thermally activated semiconducting conduction (see Fig. 3), the above scenario may not be feasible to explain LNMR in our case, because (1) our samples are single crystals with little or no grain boundaries and (2) there is no sign for cusp-shaped H dependence in MR up to 14 Tesla down to 2 K (see Fig. 4).

For $Sr_4(Ru_{1-x}Mn_x)_3O_{10}$, the observed LNMR should be related to Mn doping as it is (1) absent in $x = 0$[26,27], (2) larger in higher Mn doping level under the same condition (see Fig. 4), and (3) appearing below and above T_C. The fact that LNMR occurs in all current and field configurations with small anisotropy for both $x = 0.34$ and 0.41 indicates that it is not related to dimensional confinement nor orbital nature in our system. Similar behavior was observed in Be-doped AlGaAs – GaAs quantum well structures, in which the LNMR is attributed to spin exchange interactions between localized states[40]. Under the application of magnetic field, spin disorder related

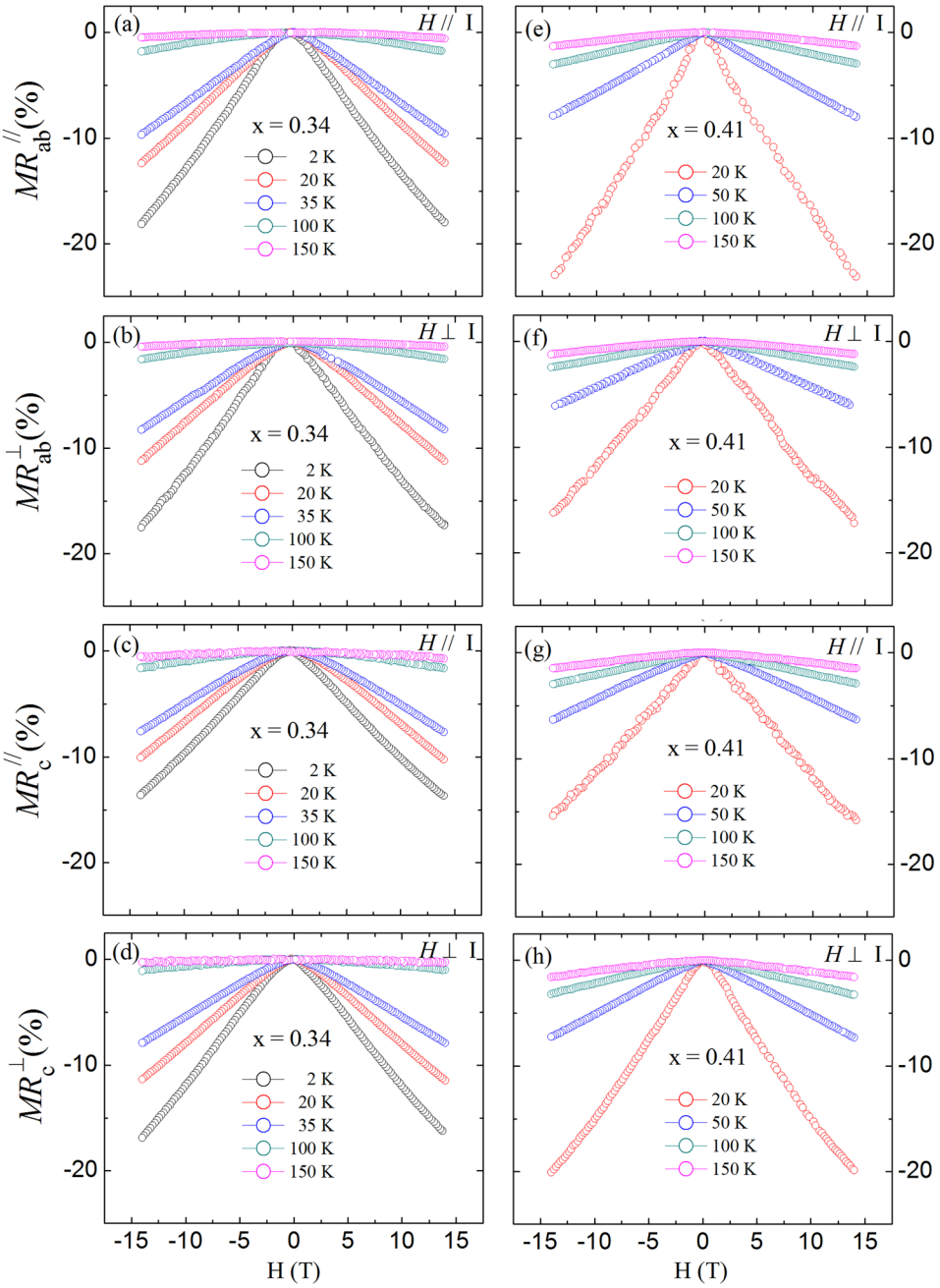

Figure 4. Magnetic field dependence of MR for $x = 0.34$ (**a**–**d**) and 0.41 (**e**–**h**) single crystals measured in the configurations of $I//ab$ and $H//I$ (**a**,**e**), $I//ab$ and $H \perp I$ (**b**,**f**), $I//c$ and $H//I$ (**c**,**g**), and $I//c$ and $H \perp I$ (**d**,**h**).

to exchange interactions is suppressed and Zeeman energy activates carriers in the localized states to delocalized states, leading to LNMR[40,45]. This is consistent with our observation that the largest LNMR occurs when H is applied along the magnetic easy (*ab*-) plane and continuous increase of magnetization (see Fig. 2). However, this scenario cannot explain the increased LNMR with increasing *x*, as energy gap is enlarged and spin polarization becomes weaker. Theoretically, MR in doped ferromagnetic semiconductors is expected to be inversely proportional to the number of charge carriers per magnetic unit cell[30]. Our data is consistent with this picture, as Mn doping results in charge localization thus reducing charge carrier density in $Sr_4(Ru_{1-x}Mn_x)_3O_{10}$.

In summary, we have successfully grown Mn-doped single crystalline $Sr_4(Ru_{1-x}Mn_x)_3O_{10}$ with *x* up to 0.41. Single crystal X-ray diffraction indicates that the partial substitution of Ru by Mn results in symmetry change from orthorhombic to tetragonal due to the removal of octahedral rotation. Both electrical and magnetic properties are changed as well. For $x = 0.34$ and 0.41, the system becomes ferromagnetic semiconducting with $T_C \sim 35$ K and energy gap ~10 meV for $x = 0.34$ and $T_C \sim 30$ K and 30 meV for $x = 0.41$, making $Sr_4(Ru_{1-x}Mn_x)_3O_{10}$ an excellent material system to study ferromagnetic semiconducting properties. One of remarkable features is its linear negative MR observed in a wide temperature and field range in all current and field configurations. Such behavior

may be explained by considering spin exchange interactions between localized states, which likely increases with increasing Mn doping. Our results shed important insights for linear MR particularly in the case of LNMR.

Methods

High-quality $Sr_4(Ru_{1-x}Mn_x)_3O_{10}$ single crystals were grown via the floating-zone technique. For making both feed and seed rods, polycrystalline $Sr_4(Ru_{1-x}Mn_x)_3O_{10}$ was first prepared by heating the mixture with the molar ratio $SrCO_3$: $[(1-x)Ru + xMnO_2] = 4$: 3 up to 1400 °C for 24 h in oxygen atmosphere with quick cool off by quenching. It is then hydrostatically pressed into cylinder-shaped rods, and further sintered at 950 °C for another 12 h in oxygen atmosphere. Single crystals were grown through melting the feed rod and moving downward with the speed of 30 mm/h. To prevent oxygen deficiency, 0.9 MPa oxygen pressure was applied during the growth. In addition, both feed and seed rods were rotated in opposite directions at 20 rpm to improve homogeneity and reduce possible impurity.

For single-crystal X-ray diffraction (XRD), a single crystal was mounted on the tip of Kapton loop, and data were collected on a Bruker Apex II X-ray diffractometer with Mo radiation K α_1 ($\lambda = 0.71073$ Å). The SMART software was used for data acquisition over a full sphere of reciprocal space with 0.5° scans in ω with an exposure time of 10 s per frame. The 2θ range extended from 0° to 80°. Intensities were extracted and corrected for Lorentz and polarization effects with the SAINT program. Numerical absorption corrections were accomplished with XPREP which is based on face-indexed absorption. The crystal structure was determined based on full-matrix least-squares methods using the SHELXTL package[46].

Physical property measurements were investigated in $x = 0.34$ and 0.41 single crystals. The magnetization was measured using the magnetic property measurement system (MPMS, *Quantum Design*), while the electrical resistivity was carried out in the physical property measurement system (PPMS, *Quantum Design*).

References

1. Maeno, Y. *et al*. Superconductivity in a layered perovskite without copper. *Nature* **372**, 532–534 (1994).
2. Grigera, S. A. *et al*. Magnetic Field-Tuned Quantum Criticality in the Metallic Ruthenate $Sr_3Ru_2O_7$. *Science* **294**, 329 (2001).
3. Crawford, M. K. *et al*. Structure and magnetism of single crystal $Sr_4Ru_3O_{10}$: A ferromagnetic triple-layer ruthenate. *Phys. Rev. B* **65**, 214412 (2002).
4. Callaghan, A., Moeller, C. W. & Ward, R. Magnetic interactions in ternary ruthenium oxides. *Inorg Chem* **5**, 1572–1576 (1966).
5. Friedt, O. *et al*. Structural and magnetic aspects of the metal-insulator transition in $Ca_{2-x}Sr_xRuO_4$. *Phys. Rev. B* **63**, 174432 (2001).
6. Ikeda, S.-I., Maeno, Y., Nakatsuji, S., Kosaka, M. & Uwatoko, Y. Ground state in $Sr_3Ru_2O_7$: Fermi liquid close to a ferromagnetic instability. *Phys. Rev. B* **62**, R6089 (2000).
7. Perry, R. S. *et al*. Metamagnetism and Critical Fluctuations in High Quality Single Crystals of the Bilayer Ruthenate $Sr_3Ru_2O_7$. *Phys. Rev. Lett.* **86**, 2661–2664 (2001).
8. Hu, B. *et al*. Structure-property coupling in $Sr_3(Ru_{1-x}Mn_x)_2O_7$. *Phys. Rev. B* **84**, 174411 (2011).
9. Chen, C. *et al*. Hidden phases revealed at the surface of double-layered $Sr_3(Ru_{1-x}Mn_x)_2O_7$. *Phys. Rev. B* **94**, 085420 (2016).
10. Matzdorf, R. *et al*. Ferromagnetism Stabilized by Lattice Distortion at the Surface of the p-Wave Superconductor Sr_2RuO_4. *Science* **289**, 746 (2000).
11. Fang, Z. & Terakura, K. Magnetic phase diagram of $Ca_{2-x}Sr_xRuO_4$ governed by structural distortions. *Phys. Rev. B* **64**, 020509 (2001).
12. Singh, D. J. & Mazin, I. I. Electronic structure and magnetism of $Sr_3Ru_2O_7$. *Phys. Rev. B* **63**, 165101 (2001).
13. Huang, Q. *et al*. Neutron Powder Diffraction Study of the Crystal Structures of Sr_2RuO_4 and Sr_2IrO_4 at Room Temperature and at 10 K. *J Solid State Chem* **112**, 355–361 (1994).
14. Huang, Q., Lynn, J. W., Erwin, R. W., Jarupatrakorn, J. & Cava, R. J. Oxygen displacements and search for magnetic order in $Sr_3Ru_2O_7$. *Phys. Rev. B* **58**, 8515 (1998).
15. Shaked, H., Jorgensen, J. D., Chmaissem, O., Ikeda, S. & Maeno, Y. Neutron Diffraction Study of the Structural Distortions in $Sr_3Ru_2O_7$. *J Solid State Chem* **154**, 361–367 (2000).
16. Weickert, F. *et al*. Missing magnetism in $Sr_4Ru_3O_{10}$: Indication for Antisymmetric Exchange Interaction. *Scientific Reports* **7**, 3867 (2017).
17. Malvestuto, M. *et al*. Electronic structure trends in the $Sr_{n+1}Ru_nO_{3n+1}$ family (n = 1, 2, 3). *Phys. Rev. B* **83**, 165121 (2011).
18. Malvestuto, M. *et al*. Nature of the apical and planar oxygen bonds in the $Sr_{n+1}Ru_nO_{3n+1}$ family (n = 1, 2, 3). *Phys. Rev. B* **88**, 195143 (2013).
19. Carleschi, E. *et al*. Double metamagnetic transition in $Sr_4Ru_3O_{10}$. *Phys. Rev. B* **90**, 205120 (2014).
20. Weickert, F. *et al*. In-depth study of the H−T phase diagram of $Sr_4Ru_3O_{10}$ by magnetization experiments. *Physica B* **536**, 634–636 (2018).
21. Cao, G., McCall, S. K., Crow, J. E. & Guertin, R. P. Ferromagnetism in $Sr_4Ru_3O_{10}$: Relationship to other layered metallic oxides. *Phys. Rev. B* **56**, R5740 (1997).
22. Ortmann, J. E. *et al*. Competition Between Antiferromagnetism and Ferromagnetism in Sr_2RuO_4 Probed by Mn and Co Doping. *Scientific Reports* **3**, 2950 (2013).
23. Mathieu, R. *et al*. Impurity-induced transition to a Mott insulator in $Sr_3Ru_2O_7$. *Phys. Rev. B* **72**, 092404 (2005).
24. Cao, G. *et al*. Itinerant ferromagnetism to insulating antiferromagnetism: A magnetic and transport study of single crystal $SrRu_{1-x}Mn_xO_3$ ($0 \leq \times < 0.60$). *Phys. Rev. B* **71**, 035104 (2005).
25. Horiba, K. *et al*. Electronic structure of $SrRu_{1-x}Mn_xO_3$ studied by photoemission and x-ray absorption spectroscopy. *Phys. Rev. B* **81**, 245127 (2010).
26. Fobes, D. *et al*. Phase diagram of the electronic states of trilayered ruthenate $Sr_4Ru_3O_{10}$. *Phys. Rev. B* **75**, 094429 (2007).
27. Fobes, D. *et al*. Anisotropy of magnetoresistivities in $Sr_4Ru_3O_{10}$: Evidence for an orbital-selective metamagnetic transition. *Phys. Rev. B* **81**, 172402 (2010).
28. Pippard, A. B. Magnetoresistance in metals. *Cambridge University Press*, Cambridge (1989).
29. Kapitza, P. The change of electrical conductivity in strong magnetic fields. *Proceedings of the Royal Society of London A* **123**, 292 (1929).
30. Majumdar, P. & Littlewood, P. B. Dependence of magnetoresistivity on charge-carrier density in metallic ferromagnets and doped magnetic semiconductors. *Nature* **395**, 479 (1998).
31. Parish, M. M. & Littlewood, P. B. Non-saturating magnetoresistance in heavily disordered semiconductors. *Nature* **426**, 162 (2003).
32. Parish, M. M. & Littlewood, P. B. Classical magnetotransport of inhomogeneous conductors. *Phys. Rev. B* **72**, 094417 (2005).
33. Pan, J., Karki, A., Plummer, E. W. & Jin, R. Doping effect on the physical properties of $Ca_{10}Pt_3As_8(Fe_2As_2)_5$ single crystals. *Journal of Physics: Condensed Matter* **29**, 485702 (2017).
34. Abrikosov, A. A. Quantum magnetoresistance. *Phys. Rev. B* **58**, 2788 (1998).
35. Abrikosov, A. A. Quantum linear magnetoresistance. *Europhys Lett* **49**, 789–793 (2000).

36. Abrikosov, A. A. Quantum linear magnetoresistance; solution of an old mystery. *Journal of Physics A: Mathematical and General* **36**, 9119–9131 (2003).
37. Dmitriev, A., Dyakonov, M. & Jullien, R. Anomalous Low-Field Classical Magnetoresistance in Two Dimensions. *Phys. Rev. Lett.* **89**, 266804 (2002).
38. Cheianov, V. V., Dmitriev, A. P. & Kachorovskii, V. Y. Anomalous negative magnetoresistance caused by non-Markovian effects. *Phys. Rev. B* **68**, 201304 (2003).
39. Sotomayor, N. M. *et al*. Negative linear classical magnetoresistance in a corrugated two-dimensional electron gas. *Phys. Rev. B* **70**, 235326 (2004).
40. Agrinskaya, N. V., Kozub, V. I., Mikhailin, N. Y. & Shamshur, D. V. Spin-controlled negative magnetoresistance resulting from exchange interactions. *JETP Lett.* **105**, 484–487 (2017).
41. Schluck, J. *et al*. Linear negative magnetoresistance in two-dimensional Lorentz gases. *Phys. Rev. B* **97**, 115301 (2018).
42. Zhang, X., Xue, Q. Z. & Zhu, D. D. Positive and negative linear magnetoresistance of graphite. *Phys Lett A* **320**, 471–477 (2004).
43. Hishiyama, Y., Irumano, H., Kaburagi, Y. & Soneda, Y. Structure, Raman scattering, and transport properties of boron-doped graphite. *Phys. Rev. B* **63**, 245406 (2001).
44. Fujita, S. Negative magnetoresistance in carbons and diffuse scattering at crystallite boundaries. *Carbon* **6**, 746–748 (1968).
45. Fukuyama, H. & Yoshida, K. Negative Magnetoresistance in the Anderson Localized States. *J.Phys. Soc. Jpn*. **46**, 102–105 (1979); ibid, **46**, 11522 (1979).
46. Sheldrick, G. M. A short history of SHELX. *Acta Crystallogr A* **64**, 112–122 (2008).

Acknowledgements

This material is based upon work supported by the U.S. Department of Energy under EPSCoR Grant No. DE-SC0016315 (LX, RJ), and Louisiana Board of Regents Research Competitiveness Subprogram (RCS) under Contract Number LEQSF(2017-20)-RD-A-08 grant for X-ray diffraction refinement (XG, WX). This research used resources at the High Flux Isotope Reactor, a DOE Office of Science User Facility operated by the Oak Ridge National Laboratory for magnetic structure refinement (HC). High-pressure floating-zone technique was employed for single crystal growth under the supervision of JY and BCS who are supported by the US Department of Energy, Office of Science, Basic Energy Sciences, Division of Materials Sciences and Engineering.

Author Contributions

R.J. designed research; L.X. synthesized the sample with assistance from J.Y. and B.C.S. and conducted physical property measurements; X.G. and W.X. carried out the single crystal XRD refinement; H.C. did magnetic properties analysis; L.X. and R.J. wrote the manuscript with the contributions from all the authors.

Additional Information

Competing Interests: The authors declare no competing interests.

Publisher's note: Springer Nature remains neutral with regard to jurisdictional claims in published maps and institutional affiliations.